High magnetic coercive field in Ca-Al-Cr substituted strontium hexaferrite

Marian Stingaciu,[a§] Durgamadhab Mishra,[b,c] César de Julián Fernández,[c] Riccardo Cabassi, [c] Anna Zink Eikeland,[d] Mogens Christensen [d] and Stefano Deledda [a,*]

[a]*Institute for Energy Technology, Instituttveien 18, NO-2007 Kjeller, Norway*

[b] *Department of Physics, IIT Jodhpur, Karwad 342037 Rajasthan, India*

[c] *Institute of Materials for Electronics and Magnetism - CNR, Parco Area delle Scienza 37/A, 43124-Parma, Italy*

[d] *Center for Materials Crystallography, Department of Chemistry and iNANO, Aarhus University Langelandsgade 140, DK-8000 Aarhus C, Denmark.*

[§] Present Address: *Center for Materials Crystallography, Department of Chemistry and iNANO, Aarhus University Langelandsgade 140, DK-8000 Aarhus C, Denmark*

* Corresponding author: stefano.deledda@ife.no

Abstract

The structural and magnetic properties of $Sr_{0.67}Ca_{0.33}Fe_9Al_{3-x}Cr_xO_{19}$ submicrometric powders with substitution levels ranging from x=0 up to x=3, prepared by sol-gel synthesis method, have been investigated. The powders were characterized by high resolution synchrotron X-ray diffraction,

scanning electron microscopy, powder neutron diffraction and MPMS-SQUID magnetometer. The structural analysis shows that upon Ca-substitution of $SrFe_{12}O_{19}$ at the Sr site and Al-Cr at the Fe sites, the magnetoplumbite structure is preserved, even for large levels of substitutions. The X-ray powder diffraction peak broadening and Williamson-Hall plots analyses indicate an increase of crystallites size and relaxation of the microstrain with increasing amounts of Chromium. The magnetic hysteresis loops reveal high coercivity fields at room temperature, with the highest value of $H_c = 1125$ kA/m (1.41 T) obtained for $Sr_{0.67}Ca_{0.33}Fe_9Al_{2.5}Cr_{0.5}O_{19}$ powder interesting to develop free-Rare Earth high coercivity magnets. The saturation magnetization and remanence values increase monotonically with increasing Cr content while the switching field decreases. The structural Rietveld refinement of combined X-ray/neutron diffraction data shows the affinity of Al^{3+} and Cr^{3+} cations to migrate mainly towards (2a) Fe-Oh2 and (12k) Fe-Oh3 sites and only minor amounts is found on the (4f1) Fe-Oh1 octahedral sites. The structural observations corroborate the magnetic properties, demonstrating a correlation between the structure and magnetic properties in Ca-Al-Cr substituted strontium hexaferrite. The role of the particle size to maximize the coercivity properties is discussed.

Keywords: Sol-gel; Magnetic Properties; Neutron Diffraction; Substituted Strontium Hexaferrite; Structure–property relationship

1. Introduction

In the past six decades, since the discovery of magnetic hard hexaferrites by scientists at Philips Laboratories in 1950s, this class of materials has received increasing attention because of its importance in technologically fields such as recording media and data storage, microwave devices, or permanent magnets industry. Continuous efforts have focused on improving the

magnetic performance by using different synthesis and processing techniques to tailor the microstructure, particle size or particle shapes at nanoscale level. Nowadays, in the field of permanent magnets, one of the most widely used class of magnetic compounds is strontium hexaferrite ($SrFe_{12}O_{19}$), which displays a moderate value of specific magnetization (σ_S) of 74 Am^2/kg (equivalent to an induction saturation of 0.47 T) a magnetic ordering temperature around 475 °C, an uniaxial magnetocrystalline anisotropy constant of 3.57×10^5 J/m^3 at room temperature [1], a magnetocrystalline anisotropy (H_A) of 1.8 T (1436 kA/m) [2], a high thermal stability and relatively good magnetic performances with respect to its production cost. Coercivity fields (H_c) in the range of 0.2-0.32 T (160-255 kA/m) are typically observed in the isotropic magnets which are strongly related to the microstructure that is highly influenced by the synthesis method [3,4].

Ferrite based magnets cover actually more than one-third of the magnets market [5] being the second market after the rare-earth (RE) magnets by their economic importance and are widespread used in less-performant magnetic applications [3]. The differences with the RE magnets are correlated with the weaker magnetic properties of M-type ferrites: the SFO exhibit smaller B_S (0.47 T), smaller H_c (<0. 4 T or 320 kA/m) and much smaller energy product, $(BH)_{max}$ (<35 kJm^{-3}) than Nd-based 2:14:1 phase-based magnets, B_S ~1.6 T, Hc< 2 T (1595 kA/m), and $(BH)_{max}$= 200-400 kJm^{-3}) [5,6]. On the other hand, the economic cost of the SFO magnets is much smaller than the RE-magnets, amplified by the RE supply crisis from the years 2010-2011 [5,7] and the high ambient cost in the extraction and transformation of RE raw materials [8]. These aspects explain the role of the ceramic magnets and motivation for improving the properties of M-type hexaferrites. For this purpose, the goal is to increase both the H_c and σ_s in order to get the increasing of the remanence and the $(BH)_{max}$. One of the most promising synthesis routes to produce isotropic strontium hexaferrites ($SrFe_{12}O_{19}$) with enhanced H_c is the sol-gel method. It

was shown that a large $\mu_0 H_c$ of about 0.66 T (526 kA/m) can be obtained in the glycol assisted sol-gel synthesis of $SrFe_{12}O_{19}$ compound [9] which is close to the theoretical value $\mu_0 H_C = 0.49\ \mu_0 H_A$ of around 0.9 T (720 kA/m) predicted by Stoner and Wohlfarth in randomly oriented single domain particles [10]. The increase of the saturation induction constitutes the major effort as implies the change of the ferrimagnetic order intrinsic to the M-type ferrites [11].

A large number of publications show the possibility of tuning the magnetic properties (magnetization and coercive force) by substituting Sr and Fe with other alkaline earth, rare earth and transition metal cations in such a way to modify the magnetization or the effective anisotropy. In a first approximation, the coercive field is proportional to the second order magnetocrystalline anisotropy constant, K_1, and inversely to the magnetization saturation, M_S. The composition-dependence of these two intrinsic properties gives rise to recently explored possibility to modulate the coercive field. Commercial magnets developed by substitution with La and Co reveal $\mu_0 H_c$ up to 0.45 T (360 kA/m) [12,13], or 0.75 T (600 kA/m) as the magnetic anisotropy is increased [14]. The same trend is observed in La-Zn substitution where a H_c value of 0.41 T (327 kA/m) could be achieved [15]. Wang et *al*. studied also the effect of rare-earth substitutions like Sm [16] or Nd [17] and found a moderate increase in H_c to 0.45 T (360 kA/m) and 0.38 T (303 kA/m), respectively. Substitution by La alone leads to a decrease of H_c as the La/Sr ratio is increased [18], whereas substitution of Fe by Cr shows an increase of H_c to 0.73 T (580 kA/m) when applying the microwave–hydrothermal synthesis method [19], or sol-gel synthesis [20]. Many other trials involving substitution with Zn-Sn [21], Sn-Mg [22], Ni-Zn [23], or Er-Ni [24] show a decrease in H_c but increase of the saturation magnetization values. Up to date, the largest H_c values observed in strontium hexaferrites were achieved for Al-substituted compounds for different synthesis methods and level of substitution. For instance, an increase of H_c up to 0.75 T (600 kA/m) was

found for nanofibers prepared by electro-spinning [25]. A more significant increase in H_c up to 1.8 T (1436 kA/m) was achieved for powders produced by sol-gel synthesis with high level of Al-substitution [26]. Very recently, Trusov *et al.* reported a record value of 2.13 T (1700 kA/m) for Ca-Al substituted powders synthesized by sol-gel. The high H_c value was attributed to a higher magnetocrystalline anisotropy caused by the crystal structure distortion resulting from the double Ca-Al substitution [27]. This remarkable high value of H_c is comparable to the values observed in the more thermodynamically unstable, ε-Fe_2O_3 phase [28]. Despite such a high H_c, the composition $Sr_{0.67}Ca_{0.33}Fe_8Al_4O_{19}$ shows a dramatic decrease of magnetization values of only 12.9 Am^2/kg.

In this study, we report the structural and magnetic properties for nanoparticles with composition $Sr_{0.67}Ca_{0.33}Fe_9Al_{3-x}Cr_xO_{19}$ ($0 \leq x \leq 3$) which were produced by sol-gel synthesis. The main goal was to investigate the adequate substitution of non magnetic Al ion by the magnetic Cr ion in order to increase the magnetization and maintain the high coercive fields. The distribution of substituted cations on the five inequivalent crystallographic sites – three octahedral ($2a$, $12k$ and $4f2$), one tetrahedral ($4f1$) and one trigonal bipyramidal ($2b$) sites – is expected to affect the magnetic properties. The magnetic structure of the parent compound ($SrFe_{12}O_{19}$) is ferrimagnetic with the spins at $12k$, $2a$ and $2b$ ferromagnetically coupled and antiferromagnetically coupled to the spins at $4f2$ and $4f1$ sites. In the ideal case the replacement of Fe^{3+} at the $4f1$ and $4f2$ sites by non-magnetic Al^{3+} would lead to a positive contribution to the total magnetization. Theoretical calculations and experimental results show that the substitution by Al^{3+} alone leads to a dramatic decrease in magnetization as Al^{3+} preferentially occupy the $2a$ and $12k$-sites giving rise to the decreasing of the saturation magnetization [29]. In this work, we explored the effect of substituting Fe^{3+} with different ratios of non-magnetic Al^{3+} and magnetic Cr^{3+}. A larger magnetic cation added into the structure of $SrFe_{12}O_{19}$ is expected to produce a rearrangement of the structure with a

5

diffusion of Al cations towards $4f1$ and $4f2$ sites, concomitant with a retention of the magnetization values. On the other hand, we employ the sol-gel technique to synthesize particles in the submicrometric range in which the reversal process can occur thorough the coherent rotation process. In this reversal regime the domain wall formation is not available and the coercive field is maximized. The single domain size corresponding to Sr and Ba hexaferrite particles is between 600 nm and 1 micron [4,6,30,31]. The corresponding single domain size in substituted hexaferrites has not been investigated. Most of the investigated doped-ferrites are grown as grains of over micrometric size, in which the domain wall is available and hence coercive field is not maximized. Here, parameters of the sol-gel route were investigated to maintain particle size in the submicrometric range.

2. Experimental methods

2.1. Sample preparation

The particles with composition $Sr_{0.67}Ca_{0.33}Fe_9Al_{3-x}Cr_xO_{19}$ ($0 \leq x \leq 3$) were synthesised by the sol-gel method using $Sr(NO_3)_2$ (98% purity), $Ca(NO_3)_2 \cdot 4H_2O$ (97%), $Al(NO_3)_3 \cdot 9H_2O$ (98%), $Fe(NO_3)_3 \cdot 9H_2O$ (98%) and $Cr(NO_3)_3 \cdot 9H_2O$ (99.9%). All chemicals used in this work were purchased from Alfa-Aesar and used as received. In a typical synthesis, the amount of nitrates were weighted according to the nominal composition $Sr_{0.67}Ca_{0.33}Fe_9Al_{3-x}Cr_xO_{19}$ (x = 0, 0.5, 1.5, 2.5 and 3), dissolved in a minimum volume of distilled water and mixed by magnetic stirring for 10 minutes. When a clear solution was obtained, citric acid ($C_6H_8O_7$) was added by keeping the molar ratio of metal cations to citric acid at 1:2. Ammonium hydroxide (NH_4OH) was added dropwise by a syringe until the pH of the solution was adjusted to 7. Afterwards, the solution was heated at 90 °C on a hot-plate and kept at a continuous stirring until the water was evaporated and

a viscous gel formed. The temperature was then gradually increased to 280 °C where a smoldering burn of the gel occurred. The products were transferred to a preheated Carbolite CWF1100 muffle furnace (500 °C), further heated to 950 °C and 1050 °C using a heating rate of 25 °C /min and calcined for 2 hours. At the end of calcination time the samples were quenched in air.

2.2. Structural characterization

The as-synthesized powders were investigated by high resolution synchrotron radiation powder X-ray diffraction (HR-PXRD). The measurements were performed at the Swiss-Norwegian Beam Line (SNBL-BM31-line), at ESRF-Grenoble, France using a fixed wavelength, λ= 0.49433 Å. The powders were packed in quartz capillaries of 0.8 mm in diameter and rotated during the measurements.

Neutron powder diffraction (NPD) was performed at room temperature using the DMC diffractometer at Paul Scherrer Institute, Switzerland. The measurements were done using un-polarized neutrons at a fixed wavelength of 2.4576 Å.

The neutron and synchrotron powder diffraction data were combined to perform structural and magnetic Rietveld refinements, which is required as the atoms with close relative scattering lengths are present in the compositions. The powder diffraction patterns were analyzed using the Jana2006 software [32]. In the refinement procedure the backgrounds of each analyzed patterns were described using a fifth degree Chebyshev polynomial. The scale factors, zero shifts, lattice parameters, site-specific occupancies and the thermal parameters were refined together with the atomic positions (x,y,z) corresponding to the iron sites. As five different iron sites are present in the structure, restrictions and linear constrains were applied in order to obtain a reliable model; A) Each site was constrained to be fully occupied, B) linear constrains were imposed to keep the

overall sum of the elements in accordance with the nominal composition and C) The atoms present on specific sites were refined to have identical coordinates and thermal parameters.

The Williamson-Hall plots method was used to determine the microstrain/size structural parameters of the powders. The peak profiles were modeled using a Thompson-Cox-Hastings function in a LeBail fitting procedure using the FullProf software [33]. The peak profiles fittings were performed including an instrumental resolution file constructed based on a silicon NIST SRM 640d standard, measured in the same configuration as for the investigated samples. Due to the intrinsically narrow instrumental contribution of the synchrotron beam line to the FWHM, the grain size could be followed up to 300 nm, whereas for a laboratory instrument the limit is typically 100 nm [34].

2.3. Electron microscopy

The particle morphology was studied by scanning electron microscope (SEM) using an ultra-high resolution Hitachi S-4800 microscope at an acceleration voltage of 15 kV. To obtain an estimation of the mean particle size, the micrographs were analyzed using the ImageJ software [35] by counting a number of about 60 particles for each composition.

2.4. Magnetic characterization

The magnetic hysteresis loops of isotropic powders were measured by a MPMS superconducting quantum interference device (SQUID) from Quantum Design up to applied field of 5 T at room temperature. The powders were dispersed in a crystalline polymer (Crystalbond™ 509) with low melting temperature to rule out any physical rotation of the particles during the magnetic measurements.

3. Results and discussion

3.1. Structural characterization of Ca-Al-Cr substituted hexaferrite

The HR-PXRD patterns of $Sr_{0.67}Ca_{0.33}Fe_9Al_{3-x}Cr_xO_{19}$ (x=0, 0.5, 1.5, 2.5 and 3.0) were collected at room temperature. The results of Rietveld refinements, shown in Figure 1(a), confirmed the formation of M-type strontium hexaferrite structure, with the space group $P6_3/mmc$ for all five samples. In addition, the high quality of the data allowed detection of minor traces of hematite impurity phase < 3.6 wt.% with the largest impurity amount observed in the compound with x=3. The amount of impurity phase detected in the powders are given in Table I. Hematite can be readily distinguished at the $2\theta=10.55°$, as well as at higher angles especially for the samples with x=2.5 and 3, as the peaks corresponding to the hexaferrite phase shift to lower 2θ values. Compared to the parent compound $SrAl_3Fe_9O_{19}$ (x = 0), it is possible to distinguish a shift of the diffraction peaks towards smaller 2θ values as the amount of Cr^{3+} is increased. Such behavior can be attributed to the larger ionic radius of Cr^{3+}(0.62 Å) than the Al^{3+}(0.53 Å) [36]. This is confirmed in Figure 1(b) which shows a linear correlation of the lattice parameters with the Cr^{3+} amount x. As x is increased, the $a=b$ and c lattice parameters continuously expand indicating that Al^{3+} are effectively substituted by larger Cr^{3+} into the structure. The lattice parameters a and c were found to increase by 0.93% and 0.48% respectively, as the substitution of Al^{3+} is complete (x=3). The evolution of c/a ratio as a function of x for the $Sr_{0.67}Ca_{0.33}Fe_9Al_{3-x}Cr_xO_{19}$ is shown in Figure 1(c). In 1974, Verstegen et *al.* showed that c/a ratio can be used to classify the type of structure [37]. It was generally observed that a ratio below 3.98 corresponds to the magnetoplumbite structure, while higher ratio leads to a distorted β-alumina structure. In this study, the c/a ratio is in the range

from 3.89 to 3.92, which confirms that the magnetoplumbite structure is preserved with the amount of Cr^{3+} substitution investigated in this work.
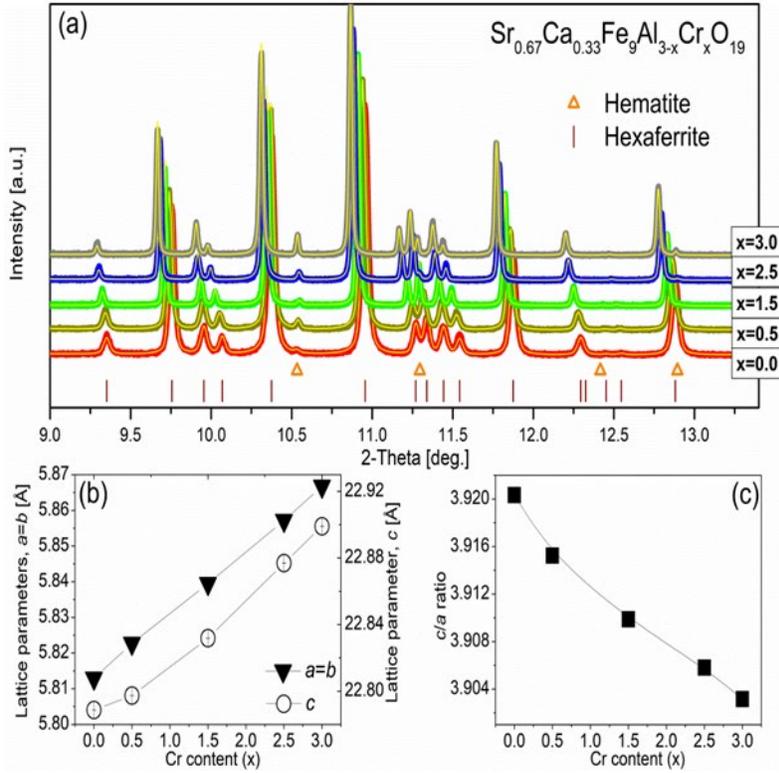

Figure 1. (a) Observed HR-PXRD patterns together with the profiles calculated by Rietveld refinement (yellow lines). (b) Evolution of lattice parameters with Cr^{3+} content, x. (c) The c/a lattice parameters ratio as a function of x.

Williamson-Hall plots (W-H) were used to determine the influence of the Cr substitution on crystallite size and microstrain from the analysis of the broadening of X-ray diffraction peaks [38]. The approach of the W-H plots relies on the principle that the strain broadening (β_ε) and crystallites size broadening (β_s) change differently with the Bragg angle θ, according to Eq.(1).

$$\beta_\varepsilon = 4\varepsilon tan\theta \ , \qquad \beta_s = \frac{K\lambda}{Scos\theta} \qquad (1)$$

If both contributions are present to the peaks broadening, then a convolution of the two can be considered, leading to equation (2).

$$\beta_{tot} = \beta_\varepsilon + \beta_s = 4\varepsilon tan\theta + \frac{K\lambda}{Scos\theta} \quad (2)$$

Multiplying by cosθ, equation (2) can be re-written as

$$\beta_{tot}cos\theta = 4\varepsilon sin\theta + K\lambda/S \quad\quad (3)$$

where S is the crystallite size, K is the Scherrer constant describing the crystallite shape factor (an overall average value of 0.9 used in this study), $\lambda = 0.49433$ Å is the used X ray wavelength and β_{tot} represents the width of the diffraction peaks given in radians, corrected for instrumental broadening. By plotting $\beta_{tot}cos\theta$ versus $4sin\theta$ and fitting linearly, the microstrain component, ε can be calculated from the slope and crystallite size component, $K\lambda/S$ from the intercept. The linear fits are depicted in Figures 2(a)-(d) and the results are presented in Table I.

For simplicity, the W-H plots given in Figures 2(b)-(c) contain only the (00l+h0l) reflections and the (hk0) reflections are omitted. The values for microstrain/size calculated from the (hk0) reflections can be found in Table I. The W-H analysis allows also to investigate the anisotropic crystal growth that exhibits this type of ferrites. In fact, a general feature observed in the M-type ferrites is the anisotropic platelet like morphology caused mainly by the different crystallite size along c crystallographic direction when compared with the crystallites size in the ab-plane [3]. This is illustrated in Figure 2(a) for sample $Sr_{0.67}Ca_{0.33}Fe_9Al_3O_{19}$ where the W-H plot corresponding to the (00l) Bragg reflections is well separated from the W-H plot of (hk0) reflections. The linear fits of the two curves gives comparable values in terms of microstrain but considerable larger crystallite size values for (hk0) reflections (see values in Table I). Crystallites with 23% increase in size along the ab plane are suggested to be the main contribution to the observed anisotropy effect. For comparison, only 5% decrease in microstrain was calculated for
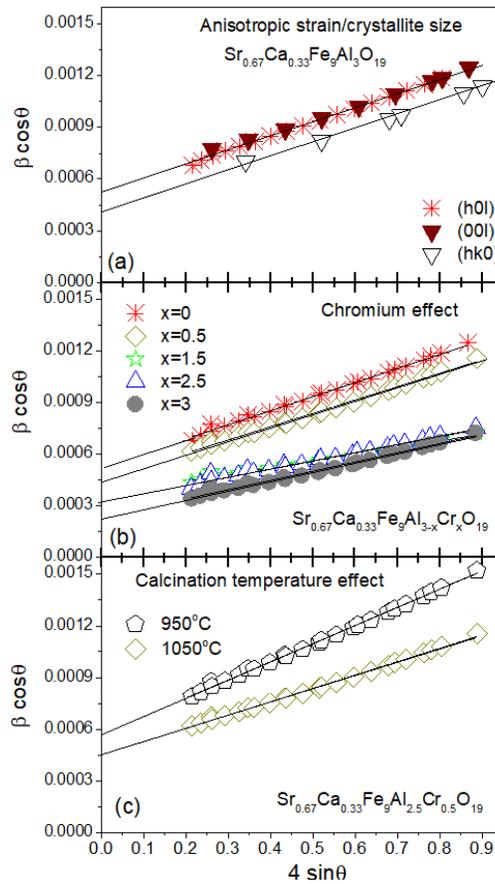
Figure 2. Williamson-Hall plots analysis on: (a) $Sr_{0.67}Ca_{0.33}Fe_9Al_3O_{19}$ samples including the ($h0l$), ($00l$) and ($hk0$) reflections; (b) Al-Cr substitution influence in $Sr_{0.67}Ca_{0.33}Fe_9Al_{3-x}Cr_xO_{19}$; c) calcination temperature effect on composition, $Sr_{0.67}Ca_{0.33}Fe_9Al_{2.5}Cr_{0.5}O_{19}$. The points shown in (b), (c) plots are given only for ($00l$) and ($h0l$) reflections.

the slope corresponding to the ($hk0$) reflections. The evolution of W-H plots for samples of $Sr_{0.67}Ca_{0.33}Fe_9Al_{3-x}Cr_xO_{19}$ (x = 0, 0.5, 1.5, 2.5 and 3.0), all calcined at 1050 °C for 2 hours, is given in Figure 2(b). For low Cr substitution level (x ≤ 0.5) the samples show a somewhat similar trend in terms of both, crystalline size and strain, but with slightly larger values of crystallites sizes for sample with x=0.5 (see Table I, below). Increasing the amount of Cr (x ≥ 1.5) leads to a change in

12

the W-H plots behavior indicating a release in lattice microstrain and a considerably crystallite growth. Figure 2(c) shows a comparison of the W-H plots obtained on sample $Sr_{0.67}Ca_{0.33}Fe_9Al_{2.5}Cr_{0.5}O_{19}$ calcined for 2 hours at temperatures of 950 °C and 1050 °C, respectively. Increasing the calcination temperature leads to a relaxation of the microstrain together with an increase in crystallite size, as reflected by higher values in the y-intercepts (values reported in the Table I).

Table 1. Weight fraction of hematite detected and change in the volume cell with different content of Al-Cr. The microstrain and crystallite size values obtained from the Williamson-Hall plots of the $(00l)/(h0l)$ and $(hk0)$ reflections are also reported. [a]All samples were calcined at 1050 °C for 2 hours, except sample Nr 7 which was calcined at 950 °C for 2 hours. More about the crystallographic parameters can be found in Table 1 and Table 2 in SI.

Nr	Sample	HR-PXRD		Williamson-Hall results			
		Hematite (wt.%)	Hexaferrite volume cell ($\mathring{A}^3$)	Strain S($hk0$) ($\times 10^{-4}$)	Strain S($00l$) ($\times 10^{-4}$)	Size ab (nm)	Size c (nm)
1	$SrFe_9Al_3O_{19}$	0.23(1)	668.089(13)	10.0(2)	10.5(1)	90(3)	77(1)
2	$Sr_{0.67}Ca_{0.33}Fe_9Al_3O_{19}$	0.40(5)	666.872(7)	7.8(2)	8.2(1)	103(4)	84(1)
3	$Sr_{0.67}Ca_{0.33}Fe_9Al_{2.5}Cr_{0.5}O_{19}$	1.20(6)	669.349(10)	7.9(2)	7.7(1)	114(5)	98(1)
4	$Sr_{0.67}Ca_{0.33}Fe_9Al_{1.5}Cr_{1.5}O_{19}$	0.78(12)	674.254(10)	3.9(2)	3.9(1)	160(9)	121(2)
5	$Sr_{0.67}Ca_{0.33}Fe_9Al_{0.5}Cr_{2.5}O_{19}$	1.82(6)	679.679(4)	4.5(2)	4.7(1)	207(16)	136(3)
6	$Sr_{0.67}Ca_{0.33}Fe_9Cr_3O_{19}$	3.62(7)	682.571(4)	5.4(2)	5.3(1)	299(36)	189(5)
7[a]	$Sr_{0.67}Ca_{0.33}Fe_9Al_{2.5}Cr_{0.5}O_{19}$	2.59(13)	670.037(31)	17.2(3)	10.5(1)	94(4)	77(1)

3.2. Morphologies of Ca-Al-Cr substituted hexaferrite

The powder morphology analysis of $Sr_{0.67}Ca_{0.33}Fe_9Al_{3-x}Cr_xO_{19}$ ($0 \leq x \leq 3$) was carried out by SEM and few representative micrographs are shown in Figures 3(a)-(e). Overall, it can be noticed that the smallest particles were synthesized for composition with no Cr added into the structure ($x = 0$), as seen in Figure 3(a). The particles are of irregular shape with a pronounced tendency for agglomeration and intergrowing. With addition of Cr to the structure ($x \geq 0.5$), one can distinguish an increase in particle size and formation of particles with mixed morphologies consisting of particles with irregular shapes and particles with well-defined platelets hexagonal shapes, which are better visible in the samples x=0.5,1.5 and x=2.5.

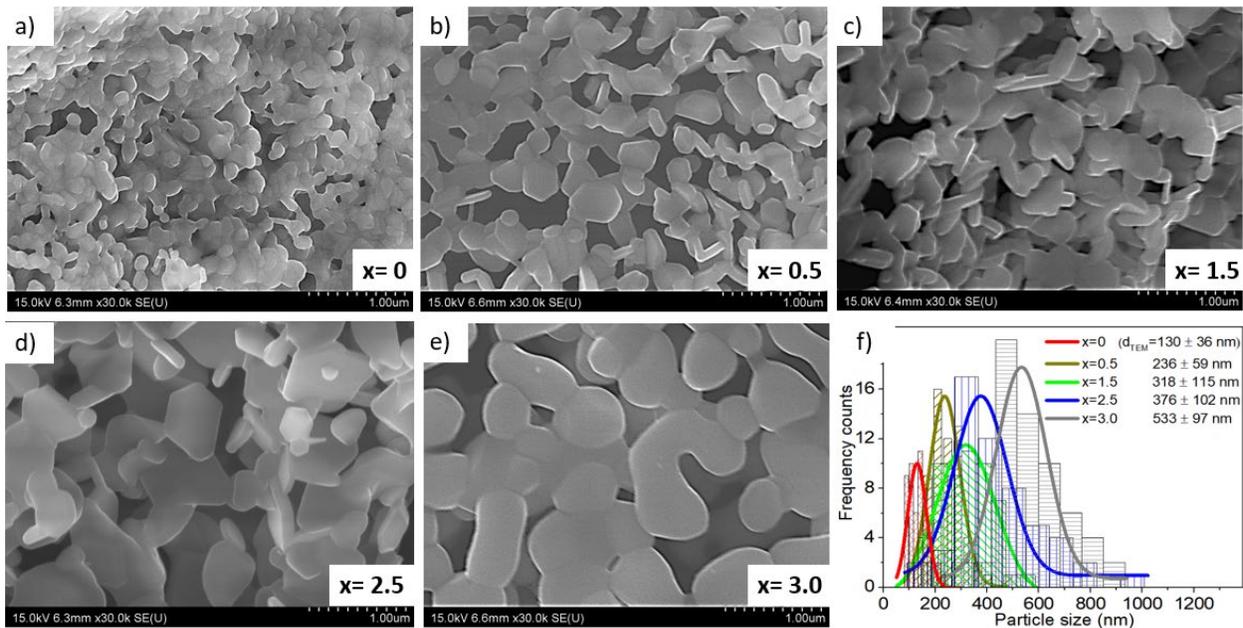**Figure 3.** SEM pictures of $Sr_{0.67}Ca_{0.33}Fe_9Al_{3-x}Cr_xO_{19}$ powders with different Cr content, x. (a) x=0; (b) x=0.5; (c) x=1.5; (d) x=2.5; (e) x=3; (f) Particle size analyses for all five compositions. The histograms were fitted by a Gaussian function shown by colored continuous lines, according to each composition. The average particles size and standard deviations are given in the inset.

Although the true size distribution might be influenced by the different spatial orientations of the particles with platelet structure the trend shows an increase in particle size with amount of Cr.

The hexagonal particles form platelets with large aspect ratio, indicating a grain growth with a shape anisotropy character. Nevertheless, it appears that for composition with $x = 3$, the particles evolved from hexagonal towards a more elongated/round shape-like particles. As the particles are of irregular shapes, in this analysis, the longest measurable distance of each particle was considered. The edge sizes of the particles (corresponding to the size in the *c*-direction) were not analyzed due to the lack of particles found in the required spatial orientation. The obtained histograms were fitted with a Gaussian peak function and results are depicted in Figure 3(f). The calculated average particle size and standard deviation values are given as well in the inset of Figure 3(f). It was found that the average particles sizes are increasing continuously with the amount of Cr-substitution. This tendency is in good agreement with the evolution of crystallite sizes determined by X-ray peak profile analysis. However, larger grain size values are obtained from the SEM analysis indicating formation of particles with more than one coherently scattering crystallite. While X-ray provides information about the undistorted regions in the material and able to distinguish between two adjacent misaligned regions, for the SEM is difficult to distinguish the boundary between such domains, considering them belonging to the same particle [39,40]. From the Gaussian fit profile, it can be observed that a narrower size distribution is obtained for the compositions with $x = 0$ and $x = 0.5$ compared with the powders where more amount of Cr ($x \geq 1.5$) is used in synthesis.

3.3. Neutron powder diffraction

A particular importance in the evolution of magnetic properties with substitution in hexaferrites is given by the degree of occupancy of substituted elements on the five inequivalent iron Wyckoff sites (three octahedral $\{2a(0,0,0); 12k(x,2x,z); 4f2(\frac{1}{3},\frac{2}{3},z)\}$, one tetrahedral $4f1(\frac{1}{3},\frac{2}{3},z')$ and one trigonal bypiramidal $2b(0,0,\frac{1}{4})$). The neutron powder diffraction patterns of $Sr_{0.67}Ca_{0.33}Fe_9Al_{3-x}Cr_xO_{19}$ (x=0, 0.5 and 1.5) were collected at 300 K and used to investigate the site affinity of Al^{3+} and Cr^{3+}. For each of the iron/chromium sites the following nomenclature was used to express the magnetic ordering and occupancies: $2a(0,0,0)$ = (2a) Fe-Oh2; $12k(x,2x,z)$ = (12k) Fe-Oh3; $4f2(\frac{1}{3},\frac{2}{3},z)$ = (4f2) Fe-Th; $4f1(\frac{1}{3},\frac{2}{3},z')$ = (4f1) Fe-Oh1; $2b(0,0,\frac{1}{4})$ = (2b) Fe-BP. In Rietveld refinements a combined two data sets (neutron and synchrotron data) were used to effectively separate the contribution of the different types of atoms to the observed diffraction peaks. As the scattering factor in X-ray is proportional to the number of electrons it was possible to distinguish the contribution of Al and Fe atoms, while from the neutron diffraction data, due to the different scattering lengths of Fe and Cr (9.45 fm and 3.635 fm) the two elements are distinguishable. At room temperature all magnetic contributions were found to correspond to a propagation vector $\mathbf{k}$ = [0 0 0] and the best fit to the experimental data was obtained within the hexagonal $P6_3/mm'c'$ magnetic space group. The resulting magnetic structures for the samples with x = 0 and 1.5 are given in Figures 4(a) and 4(b). The magnetic structure is collinear with the magnetic moments of Fe and Cr pointing along c-crystallographic axis. The antiparallel alignment of the spins at the (4f1) Fe-Oh1 and (4f2) Fe-Th sites causes the structures to be of ferrimagnetic ordering. For the unsubstituted sample (x = 0) the magnetic moments of Fe atoms lies in the range 3.79(10) - 2.62(13) μ_B with the larger value corresponding to the atoms confined to the (2b) Fe-BP and (4f1) Fe-Oh1 sites and smaller in the (12 k) Fe-Oh3 site. When Al^{3+} is substituted by Cr^{3+}

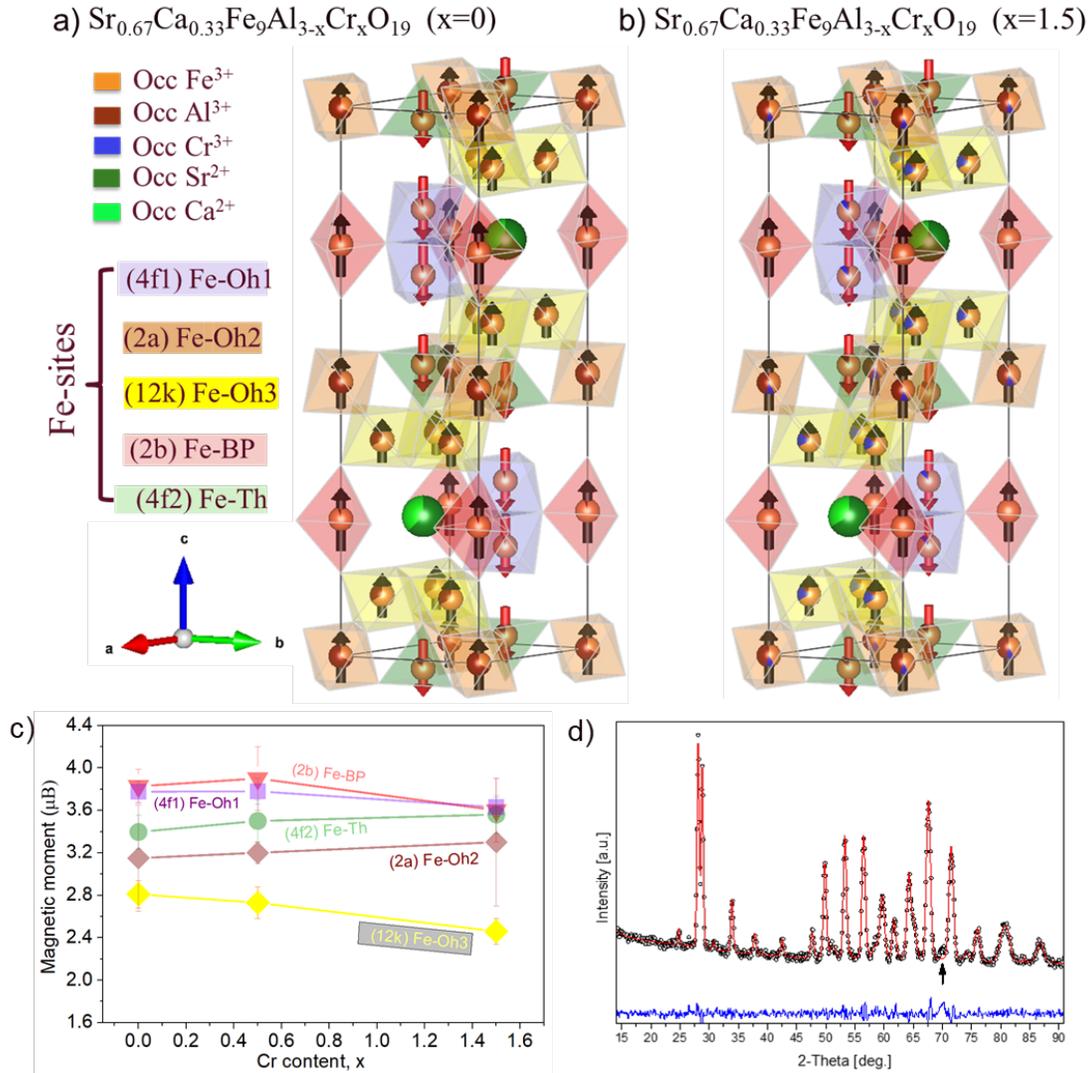there is a change in the average values of magnetic moments and the evolution is shown in Figure 4(c).

Figure 4. The refined crystal and magnetic structures of $Sr_{0.67}Ca_{0.33}Fe_9Al_{3-x}Cr_xO_{19}$. (a) x=0, (b) x=1.5. The occupation fractions for each element are indicated by the color-coded (brown/goldish/blue) spheres. The green spheres illustrate the Sr/Ca atoms while the oxygen atoms are not shown. (c) The evolution of magnetic moments modulus per atom, at each site, function of Cr substitution. (d) The final refinement of neutron diffraction pattern corresponding to the sample with x=1.5 measured at 300 K with a neutron wavelength of 2.4576 Å. Black dots represent

the measured data, red is the calculated line according to the magnetic model and blue is the difference between the two. Notice the unidentified extra peak around $2\theta=70°$ region, which was excluded in the refinements. This is a typical feature seen for all three investigated samples. The corresponding magnetic structure for the sample $Sr_{0.67}Ca_{0.33}Fe_9Al_{2.5}Cr_{0.5}O_{19}$ is shown in Figure S1 (SI).

The magnetic moments were obtained by using the Fe^{3+} and Cr^{3+} form factors and then refining the average moment of each site. The refinement of site occupancies for the sample x=0 clearly demonstrates the affinity of Al^{3+} to migrate mainly towards (2a) Fe-Oh2 and (12k) Fe-Oh3 sites. Only small fractions are found on the other three sites, as indicated in Figure 4(a). This comes in good agreement with previously work performed by Kazin on a lower level aluminum substitution of strontium hexaferrite [41]. The preference of the nonmagnetic Al^{3+} towards these specific sites would imply a decrease in net magnetization values as a diminishing contribution to the parallel configuration occurs. Indeed, this could be observed from the macroscopic magnetization measurements (Figure 4(a)) where values of 23 Am^2/kg were obtained for sample with x = 0. This is much lower compared to the parent compound $SrFe_{12}O_{19}$ which has a value of 67 Am^2/kg (see Figure S2 in SI). Once the Al^{3+} is substituted by Cr^{3+} in sample x=0.5, it can be distinguished an increase of the magnetic moments on all magnetic sites, but except for the site (4f1) Fe-Oh1 that shows a slightly decrease, which might be related to a redistribution of the Al atoms at the Fe-Oh1 which is slightly more populated for the sample with x=0.5 when compared with the sample with x=0. By adding more chromium in the structure (x = 1.5), it is easily observed that the Cr atoms prefer the (12k) Fe-Oh3, (2a) Fe-Oh2 and (4f1) Fe-Oh1 sites, as observed from Figure 4(b), and no Cr is found on the (2b) Fe-BP. The trend is valid for both compositions x=0.5 and x=1.5. With the addition of Cr the most populated sites with Al are still the (2a) Fe-Oh2 and

(12k) Fe-Oh3, but a gradual decrease in the occupied fraction is observed as the x is increased to 1.5. For the other 3 sites the Al content remains almost unchanged with the amount of Cr but still one can remark a slight increase of the Al fraction at the (2b) Fe-BP site for the sample with x=1.5, which can explain the lower magnetic moment observed at this site. More about the refined occupancies and structural parameters can be found in Table 2 included in the SI.

The bond length and bond angles for the $Sr_{0.67}Ca_{0.33}Fe_9Al_{3-x}Cr_xO_{19}$ samples with x=0, 0.5 and 1.5. were extracted from the combined Rietveld refinement and the values are reported in Table 2, for various Fe-crystallographic sites. A carefully examinations of the values indicate that the larger variations in bond-lengths with increasing amount of chromium takes place mainly at the Fe-Oh3 site, which is the preferred occupational site by the chromium. It is observed that a slight increase of all bond lengths (FeOh3-O1, FeOh3-O2, FeOh3-O4, FeOh3-O5) occurs as the chromium amount is increased, suggesting that Fe-Oh3 octahedron possesses a larger volume for the sample x=1.5. Consequently, one can interpret that the strain release observed in the W-H plots analysis might relate to a decrease of octahedral Fe-Oh3 strain, as x increases to 1.5. The angles around the different Fe-sites given in Table 2 do not change considerable with the amount of chromium, which imply that no rotation or tilting of the octahedral, tetrahedral o trigonal bipyramidal sites occurs.

Table 2. Bond lengths and bond angles from combined Rietveld refinement for the $Sr_{0.67}Ca_{0.33}Fe_9Al_{3-x}Cr_xO_{19}$ samples with x=0, 0.5 and 1.5. The larger bond length variations values with amount of x, are bolded in the table.

	Bond length (Å)				Bond angle (deg.)		
Bonding type	x=0	x=0.5	x=1.5	Bonding type	x=0	x=0.5	x=1.5
				FeOh2-O4-FeTh	125.60(2)	125.33(7)	125.27(14)
FeOh2-O4	1.942(6)	1.961(6)	1.965(4)	FeOh2-O4-FeOh3	96.60(3)	95.97(3)	96.07(10)

FeBP-O3	1.841(8)	1.842(8)	1.859(5)	FeBP-O3-FeOh1	137.88(17)	138.03(16)	138.03(19)
FeTh-O2	1.905(7)	1.899(8)	1.896(5)	FeTh-O2-FeOh3	125.96(17)	125.96(17)	126.10(10)
FeTh-O4	1.895(7)	1.887(7)	1.896(4)	FeTh-O4-FeOh3	120.1(4)	120.83(5)	120.67(10)
FeOh1-O3	2.042(6)	2.044(6)	2.034(4)	FeOh1-O3-FeOh1	84.2(3)	83.9(3)	83.94(19)
FeOh1-O5	1.981(7)	1.97(10)	1.978(4)	FeOh1-O5-FeOh3	126.6(2)	126.6(5)	126.8(3)
FeOh3-O1	**1.94 (4)**	**1.946(4)**	**1.948(2)**	FeOh3-O1-FeOh3	98.5(3)	98(3)	98.4(6)
FeOh3-O2	**2.049(5)**	**2.059(5)**	**2.065(3)**	FeOh3-O2-FeOh3	89(2)	89(2)	88.8(5)
FeOh3-O4	**2.083(4)**	**2.083(9)**	**2.087(2)**	FeOh3-O4-FeOh3	89.79(10)	89.6(7)	89.94(11)
FeOh3-O5	**1.872(8)**	**1.889(11)**	**1.895(4)**	FeOh3-O5-FeOh3	100.2(3)	99.6(8)	99.36(16)

3.4. Magnetic characterization of Ca-Al-Cr substituted hexaferrite

The magnetic hysteresis loops of the Ca-Al-Cr substituted samples are shown in Figure 5(a). The shapes of the curves of the samples with x=0 to 2.5 resemble typical randomly oriented domains with Mr/Ms ratio of about 0.5. The sample with x = 3 shows a more square loop with higher M_r/M_s ratio, indicating a different reversal process. The specific magnetization measured at 5 T (M_s), the remanent magnetization at zero field, M_r, and the coercive field, H_c, are plotted in Figure 5(b) with respect to Cr content.

Specific magnetization exhibits an almost continuous increase as Cr substitutes Al and is in all cases smaller than the value of the unsubstituted ferrite $SrFe_{12}O_{19}$ (σ_s = 75-65 Am^2/kg). This can be understood by considering the observed Ca-Al-Cr substitution. As shown by neutron diffraction analysis, for x=0, out of five distinct Fe^{3+} sites, Al^{3+} prefers 2*a* and 12*k* octahedral sites. This leads to a decrease of the total magnetic moment of the parallel sites (2a, 2b and 12k sites) in comparison to the antiparallel sites (4f1 and 4f2) for which the occupancy remains almost unchanged. Analyzing the magnetization saturation (M_s) that is equal to σ_s ×ρ, where ρ is the experimental density, we observe a reduction of M_s of 33% with respect to $SrFe_{12}O_{19}$. These

results confirm previous experimental and theoretical observations [27,29]. On the other hand, M_s increases monotonically with increasing Cr content. This is expected as Cr is magnetic and it substitutes to Al at the 2a and 12 k sites. Neutron magnetization values (σ_{NPD}) for the samples with x=0, 0.5 and 1.5 were calculated and tabulated together with the macroscopic magnetization values (σ_r and σ_s) in Table 3. The σ_{NPD} values were obtained based on the refined magnetic moments which were summed over all sites in one-unit cell and divided by the mass of unit cell. Differences between the macroscopic magnetization values and the ones obtained from neutron data are visible across the three samples. A possible reason for this can be related to the sensitivity and way of how the two techniques probe the magnetism, as well as to the unaccounted effects like e.g. the role of magnetism coming from the small amounts of hematite present in these samples. This was not considered in this work, as our main focus was to study the sites affinities for the different atomic species. Nevertheless, one can observe a good agreement in the trend of macroscopic magnetization values with the ones obtained from neutron refinement, which all increase with increasing amount of chromium.

Table 3. Magnitude of the magnetizations obtained from macroscopic (σ_r and σ_s) and neutron powder diffraction (σ_{NPD}).

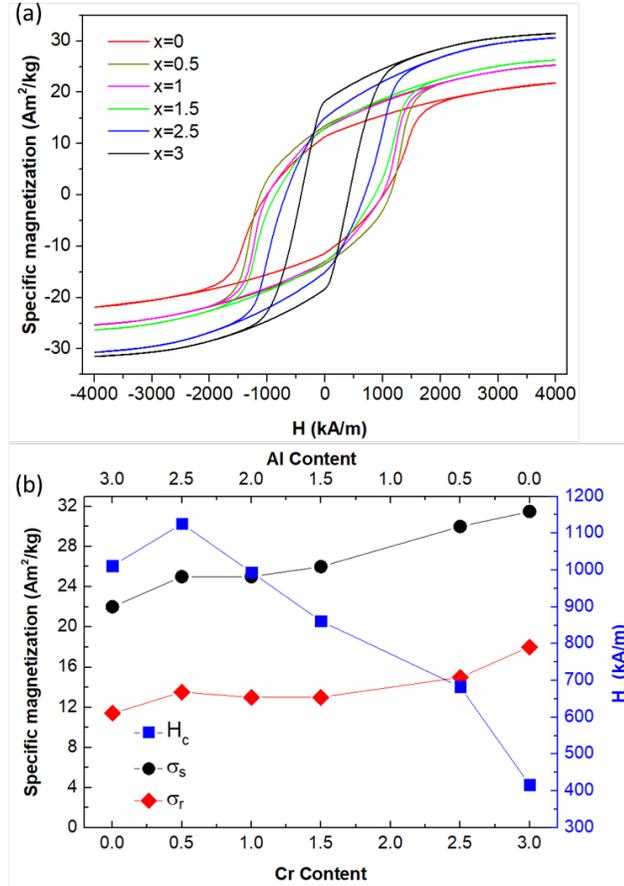| $Sr_{0.67}Ca_{0.33}Fe_9Al_{3-x}Cr_xO_{19}$	σ_r (Am^2/kg)	σ_s (Am^2/kg)	σ_{NPD} (Am^2/kg)
x=0	11.4	22	17(2)
x=0.5	13.5	25	23(1)
x=1.5	13.0	26	28(2)

Figure 5. (a) Hysteresis loops of Al-Cr substituted samples measured at 300 K. (b) Evolution of specific magnetization, remanence and coercive field with Cr content, x.

The substitution effect on the coercive field exhibits a different behavior. The initial value of the Al substituted strontium hexaferrite, $Sr_{0.67}Ca_{0.33}Fe_9Al_3O_{19}$, is more than doubled than that for the unsubstituted $SrFe_{12}O_{19}$, that is $H_c = 957.2$ and 419 kA/m, respectively. For the Cr-substituted samples, H_c values exhibit a maximum of 1125 kA/m for x=0.5 and it decreases monotonically with increasing Cr content. This indicates that Al^{3+} substitution leads to an increase in the anisotropy field or a reduced saturation magnetization. Previous experimental investigation of Cr-substituted $BaFe_{12-x}Cr_xO_{19}$ ($0 \leq x \leq 1$) performed by Qui et al. also showed a decrease in anisotropy and H_c with increasing Cr content [42]. Using Mössbauer spectroscopy, they observed

that Cr^{3+} goes to 2*a* site leading to a quadrupole splitting of 2*a* and 4*f*1 site. This should result in the reduction of the magnetic anisotropy and hence of the coercive field. To analyze this aspect in greater detail the derivative of magnetization versus the applied field were calculated so that the switching field distributions can be determined. This is shown in Figure 6(a). For low Cr content, two peaks can be observed: a small peak at the lower branch of the magnetic field and a sharper peak at higher field. Moreover, the distribution (represented by the peak width) also increases with increasing Cr content. A broader width implies a distribution in particle size (domain size) or presence of chemical inhomogeneity in the samples. The broadening of width increases with increasing Cr content, which suggests that the inhomogeneity in size and chemical state increases with higher Cr content. This can be correlated to the increase of the particle size distribution with increasing Cr substitution observed in the SEM characterizations. The maximum of the switching field, H_{SW}, corresponds to the field at which there is a more efficient reversal process. Figure 6(b) shows the composition dependence of the H_{SW}, as well as the H_C, for comparison. The H_{SW} decreases continuously with the substitution of Al^{3+} by Cr^{3+} confirming the observations of Qui et al. [42]. The maximum H_{SW}, 1405.5 kA/m, corresponds to the sample with no Cr, but the H_{SW} for the other composition remains high, above 800 kA/m, except for the sample with x=3 in which the H_{SW} is halved.
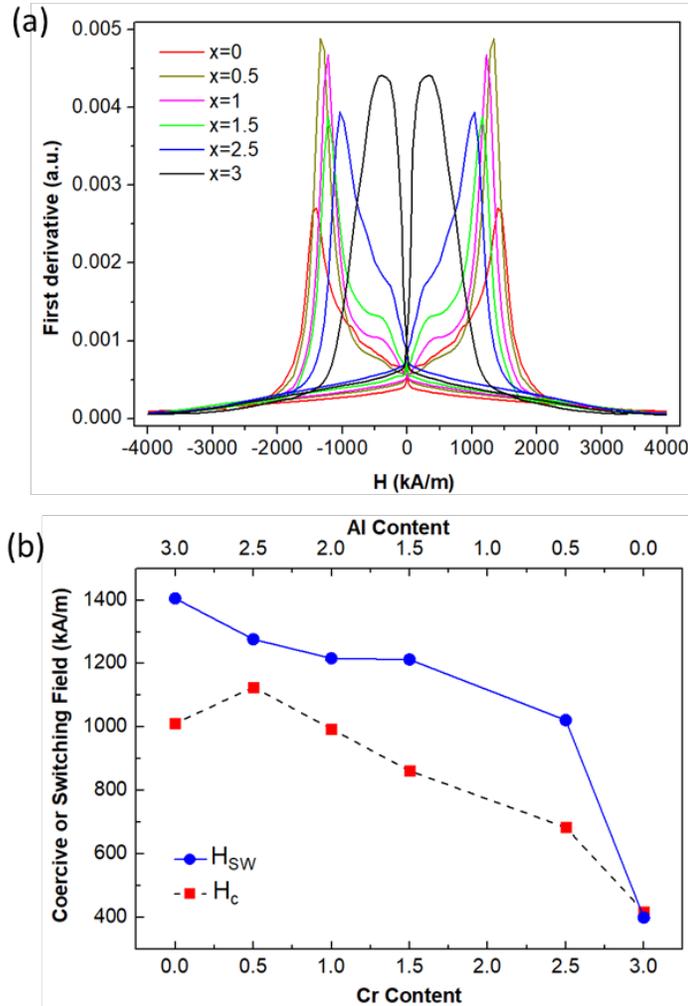
Figure. 6 (a) First derivative of hysteresis (switching field distribution). (b) Evolution of switching field and the coercive field with Cr content.

The variation of the H_{SW} (and H_C) as function of the Cr substitution could be correlated, on one hand, to the influence of the structure, the microstructure, and the morphology as well as the interparticle interactions in the reversal process. On the other hand, it can be related to changes in the magnetocrystalline anisotropy due to the structural and magnetostructural changes.

Considering the ensemble of samples, the one with x=3 exhibits different magnetic properties than the rest: the ration σ_r/σ_s is larger, there is a broad and single switching field distribution, and the values for H_C and H_{SW} drop with respect to the samples with smaller Cr. Such

difference could be correlated to the larger particle size and platelet morphology of the sample with largest Cr content. The platelet morphology gives rise to a smaller anisotropy than spherical particles due to the competition of magnetocrystalline and shape anisotropies typical of M-type hexaferrites [43]. In fact, this is corroborated by the crystallite size analysis obtained by XRD, as there is an increase in crystallite size with increasing Cr content up to 300 nm in the *ab*-plane and 189 nm in the *c*-direction (Table 1).

The differences in the behavior of low and high Cr-content could be also related to a different reversal process and could possibly stem from the different particle size, rather than particle morphology and shape. In particular, one can take into account the so-called single domain size which is the threshold between smaller monodomain and larger multidomain particles. For undoped Sr-ferrite the calculated single domain size is around 600 nm [44], but single domain behavior has been observed in particles larger than 600 nm and up to 1 μm [45]. In this work, the particles of the sample with x=3 are much larger (550 nm) than the particles of other composition (below 350 nm down to 100 nm). It can be then assumed the particles of the samples with Cr content between x = 0 and 2.5 are in the single domain regime, while the particles with larger Cr content are multidomain. In this scenario, the larger coercive fields and the σ_r/σ_s near 0.5 for low-Cr content samples may be an indication that their reversal process is driven by coherent rotation mode [46], which is typically observed in monodomain particles, while the demagnetization process for the multidomain particles of the sample with the largest Cr (x = 3) is governed by the domain wall structure and pinning mechanism.

Considering the above discussion, the effective magnetic anisotropy (K_{eff}) can be calculated assuming an uniaxial anisotropy type and considering the Stoner -Wolfarth model to describe the

reversal process. This correlates the coercive field, here the switching field, with an intrinsic properties such as the magnetic anisotropy according to

$$K_{eff} = H_{SW} \times M_S \qquad (4)$$

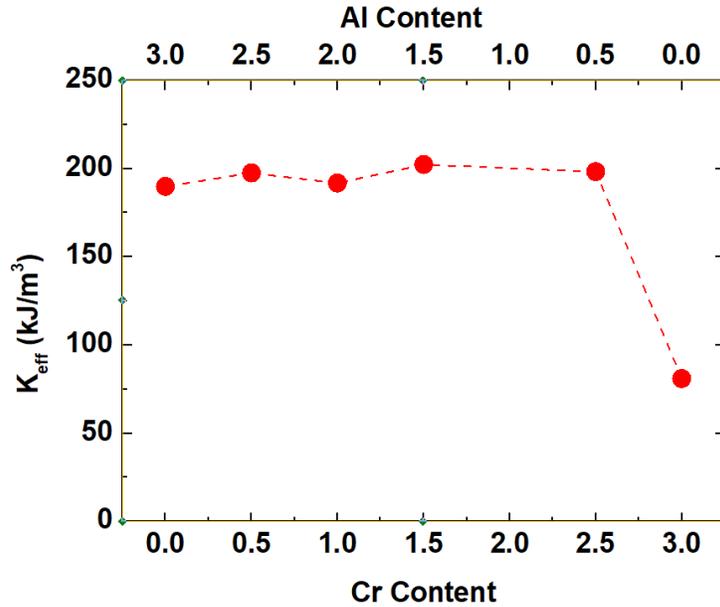The K_{eff} values are plotted in Figure 7 as function of the Cr content.

Figure 7. Evolution of effective anisotropy with Cr content.

The K_{eff} shows almost constant values around $2 \cdot 10^5$ Jm^{-3} for all compositions, except for x=3 for which a drop by more than 1/3 is observed. We should stress that K_{eff} is neither the real effective anisotropy nor the magnetocrystalline anisotropy (H_A) but it is an empirical value that allows to compare the anisotropy properties between similar compounds. The K_{eff} can represent the composition evolution of H_A even if its value could be much smaller. In fact, for the unsubstituted Sr ferrite the H_A is 1436 kA/m (1.8 T) while the measured H_C is 400 KA/m (0.5 T). The bulk K_1 is equal to $3.5 \cdot 10^5$ Jm^{-3}, the calculated K_{eff} is $2.3 \cdot 10^5$ Jm^{-3} [1]. Considering the evolution of K_{eff} as function of the composition, it can be concluded that the variation of the H_{SW}

is likely due to the change of the M_s. In addition, the results from neutron diffraction data can be taken into account. In fact, they suggest that the substitution of Al^{3+} by Cr^{3+} does not change the occupancy of 2b bipyramidal sites, where symmetry would lead to the single ion anisotropy. We also observe experimentally that the change of the lattice parameter with the composition does not affect the magnetic anisotropy. On the other hand, the change in the occupancy in the $2a$ and $12k$ sites results in an increase of the magnetization and a corresponding change of the switching field.

Of all the investigated samples, the $Sr_{0.67}Ca_{0.33}Fe_9Al_{2.5}Cr_{0.5}O_{19}$ submicrometric particles exhibit the most promising magnetic characteristics for free rare earth magnets: a high coercivity of H_C= 1125 kA/m (1.41 T), σ_s =25 Am/kg and σ_r =13.5 Am/kg.

Conclusion

A sol-gel synthesis method was successfully applied in the synthesis of triple substituted strontium hexaferrite magnetic particles. The extent of iron substitution by aluminum and chromium ions plays a determining role in tuning the structural and magnetic properties. The X-ray, structural and peak profile analysis, demonstrate the changes in the morphology, in the crystallite size and in the microstrain of the particles with the composition changes. The microstrain in $Sr_{0.67}Ca_{0.33}Fe_9Al_{3-x}Cr_xO_{19}$ ($0 \leq x \leq 3$) is more present at lower Cr substitution rates, while for substitutions larger than $x \geq 1.5$ the growth of crystallites size becomes the predominant effect. The morphology of particles changes gradually, depending on the level of substitution, from particles with an irregular shape for low Cr content towards platelets-like particles, with well-defined hexagonal shape. The change is accompanied by a larger particle size distribution as the stoichiometric amount of Cr exceeds 1.5. The magnetic hysteresis loops recorded at room temperature shows values of saturation magnetization and coercivity field which are strongly

related to the Al-Cr substitution levels. By substitution with chromium it was possible to gradually increase the saturation magnetization and maintain, or even increase the coercivity fields up to 1125 kA/m for the sample with $x = 0.5$. This corresponds to about 2.3 times larger values compared to the unsubstituted $SrFe_{12}O_{19}$ powder. However, the specific saturation magnetization reached for this composition (25 Am^2/kg) is lower than unsubstituted $SrFe_{12}O_{19}$ (65 Am^2/kg), while slightly larger than for the Al-only substituted sample. The sol-gel route allows to get successfully substituted ferrites with submicrometric sizes that maximize the values of the coercive field.

Declaration of Competing Interest

The authors declare no competing financial interests or personal relationships that could influence the work reported in this paper.

Acknowledgments

Supplementary materials

Supplementary Information is available and contains:

- Figure S1: The crystal and magnetic structure of sample $Sr_{0.67}Ca_{0.33}Fe_9Al_{2.5}Cr_{0.5}O_{19}$.

- Figure S2: Hysteresis loops of $SrFe_{12}O_{19}$ and $SrFe_9Al_3O_{19}$.

- Figure S3: Hysteresis of $Sr_{0.67}Ca_{0.33}Fe_9Al_{2.5}Cr_{0.5}O_{19}$ annealed at 950 °C and 1050 °C.

- Figure S4: Hysteresis of samples with and without Ca substitution and their switching field distributions.

- Figure S5: Magnetic susceptibility as function of temperature for $Sr_{0.67}Ca_{0.33}Fe_9Al_{2.5}Cr_{0.5}O_{19}$ and $Sr_{0.67}Ca_{0.33}Fe_9Al_2Cr_1O_{19}$.

- Table S1. Crystallographic parameters of Sr0.67Ca0.33Fe9Al3-xCrxO19 (x=0, 0.5, 1.5, 2.5, 3.0).

- Table S2. The atomic coordinates and refined occupancies of Sr0.67Ca0.33Fe9Al3-xCrxO19 (x=0, 0.5, 1.5).

References

[1] B.T. Shirk, W. R. Buessem **Temperature Dependence of M_s and K_1 of $BaFe_{12}O_{19}$ and $SrFe_{12}O_{19}$ Single Crystals** J. Appl. Phys., 40 (1969), p. 1294

[2] F. Bolzoni, R. Cabassi **Review of singular point detection techniques** Physica B, 346-347 (2004), pp. 524 – 527

[3] R.C. Pullar **Hexagonal Ferrites: A Review of the Synthesis, Properties and Applications of Hexaferrite Ceramics** Progress in Materials Science, 57 (2012), pp. 1191–1334

[4] H. Kojima **Fundamental properties of hexagonal ferrites with magnetoplumbite structure. Chapter 5 in "Ferromagnetic Materials"**. North-Holland, 3 (1982), pp. 305-392

[5] O. Gutfleisch, M.A. Willard, E. Brück, C.H. Chen, S.G. Sankar, J.P. Liu Magnetic **Materials and Devices for the 21st Century: Stronger, Lighter, and More Energy Efficient** Adv. Mater., 23 (2011), pp. 821–842

[6] J.M.D. Coey **Magnetism and Magnetic Materials**, Cambridge Univ. Press (2010)

[7] L.H. Lewis, F. Jiménez-Villacorta **Perspectives on Permanent Magnetic Materials for Energy Conversion and Power Generation**, Metall. Mater. Trans. A, 44 (2013), pp. 2-20

[8] J.C.K. Lee, Z. Wen **Rare Earths from Mines to Metals**, Journal of Industrial Ecology, 21 (2016), pp. 1277-1290

[9] X.F. Pan, G.H. Mu, N. Chen, K.K. Gan, K. Yang, M.Y. Gu **Improved properties of $SrFe_{12}O_{19}$ synthesised by gel self-propagating combustion technique with glycol as solvent** Materials Science and Technology, 23:7 (2007), pp. 865-868

[10] E.C. Stoner, E. P. Wohlfarth **A mechanism of magnetic hysteresis in heterogeneous alloys** Philos. Trans. R. Soc., 240 (1948), pp. 599-642

[11] J. M.D. Coey **Permanent magnets: Plugging the gap** Scripta Materialia, 67 (2012), pp. 524–529

[12] F. Kools, A. Morela, R. Grossinger, J.M. Le Breton, P. Tenaud **LaCo-substituted ferrite magnets, a new class of high-grade ceramic magnets; intrinsic and microstructural aspects** Journal of Magnetism and Magnetic Materials, 242–245 (2002), pp. 1270–1276

[13] P. Tenaud, A. Morel, F. Kools, J.M. Le Breton, L. Lechevallier **Recent improvement of hard ferrite permanent magnets based on La–Co substitution** Journal of Alloys and Compounds, 370 (2004), pp. 331–334

[14] D.H. Choi, S.W. Lee, In-Bo Shim, C.S. Kim **Mossbauer studies for La-Co substituted strontium ferrite** Journal of Magnetism and Magnetic Materials, 304 (2006), pp. e243–e245

[15] X. Liu, J. Bai, F. Wei, Z. Yang, S. Takei, A. Morisako, M. Matsumoto **Magnetic and crystallographic properties of La–Zn substituted Sr-ferrite thin films** J. Appl. Phys., 87 (2000), p. 6875

[16] J.F. Wang, C.B. Ponton, I.R. Harris **A study of the magnetic properties of hydrothermally synthesised Sr hexaferrite with Sm substitution** Journal of Magnetism and Magnetic Materials, 234 (2001), pp. 233–240

[17] J.F. Wang, C.B. Ponton, I.R. Harris **A study of Nd-substituted Sr hexaferrite prepared by hydrothermal synthesis** IEEE Trans. Magn., 38 (2002) pp. 2928-2930

[18] J.F. Wang, C.B. Ponton, R. Groessinger, I.R. Harris **A study of La-substituted strontium hexaferrite by hydrothermal synthesis** Journal of Alloys and Compounds, 369 (2004), pp. 170–177

[19] S. Katlakunta, S.S. Meena, S. Srinath, M. Bououdina, R. Sandhya, K. Praveena

Improved magnetic properties of Cr^{3+} doped $SrFe_{12}O_{19}$ synthesized via microwave hydrothermal route Materials Research Bulletin 63, (2015), pp. 58–66

[20] T.T.C. Trudel, J. Mohammed, H.Y. Hafeez, B.H. Bhat, S.K. Godara, A.K. Srivastava **Structural, Dielectric, and Magneto-Optical Properties of Al-Cr Substituted M-Type Barium Hexaferrite** Phys. Status Solidi A, 216 (2019), p. 1800928(1-9)

[21] A. Ghasemi, V. Šepelák, X. Liu, A. Morisako **The role of cations distribution on magnetic and reflection loss properties of ferrimagnetic SrFe$_{12-x}$(Sn$_{0.5}$Zn$_{0.5}$)$_x$O$_{19}$** J. Appl. Phys., 107 (2010), p. 09A734

[22] A. Davoodi, B. Hashemi **Magnetic properties of Sn–Mg substituted strontium hexaferrite nanoparticles synthesized via coprecipitation method**. Journal of Alloys and Compounds, 509 (2011), pp. 5893–5896

[23] S.N. Widyastuti, A. Marsha Alviani, M.R. Dwi Febri, P.V. Mitha, **Ni and Zn Substituted M-type Barium Hexaferrite Processed by Sol–Gel Auto Combustion Method** Journal of Physics: Conference Series, 877 (2017), p. 012015

[24] M.N. Ashiq, M.J. Iqbal, M. Najam-ul-Haq, P.H. Gomez, A.M. Qureshi **Synthesis, magnetic and dielectric properties of Er–Ni doped Sr-hexaferrite nanomaterials for applications in High density recording media and microwave devices**. J. Magn. Magn. Mater., 324 (2012), pp. 15-19

[25] M. Liu, X. Shen, F. Song, J. Xiang, X. Meng **Microstructure and magnetic properties of electrospun one-dimensional Al^{3+}-substituted SrFe$_{12}$O$_{19}$ nanofibers**. Journal of Solid State Chemistry, 184 (2011), pp. 871–876

[26] H. Luo, B. K. Rai, S. R. Mishra, V. V. Nguyen, J. P. Liu **Structural, Magnetic, and Electrical Properties of RE Doped Sr$_{0.82}$RE$_{0.18}$Fe$_{12-x}$Al$_x$O$_{19}$ (RE = Gd, Pr, Sm) Compound** Journal of Magnetism and Magnetic Materials, 324 (2012), pp. 2602–2608

[27] L.A. Trusov, E.A. Gorbachev, V.A. Lebedev, A.E. Sleptsova, I.V. Roslyakov, E.S. Kozlyakova, A.V. Vasiliev, R.E. Dinnebier, M. Jansen, P.E. Kazin **Ca-Al double-substituted strontium hexaferrites with giant coercivity** Chem. Commun., 54 (2018), pp. 479-482.

[28] J. Tucek, R. Zboril, A. Namai, S. Ohkoshi **ε-Fe2O3: An Advanced Nanomaterial Exhibiting Giant Coercive Field, Millimeter-Wave Ferromagnetic Resonance, and Magnetoelectric Coupling** Chem. Mater., 22 (2010), pp 6483-6505

[29] V. Dixit, C.N. Nandadasa, Seong-Gon Kim, S. Kim, J. Park, Yang-Ki Hong, L.S.I. Liyanage, A. Moitra **Site occupancy and magnetic properties of Al-substituted M-type strontium hexaferrite** J. Appl. Phys., 117 (2015), pp. 243904-1- 243904-7

[30] J.M. González, C. de Julián, A.K. Giri, S. Castro, M. Gayoso, J. Rivas **Magnetic viscosity and microstructure: Particle size dependence of the activation volume** J. Appl. Phys., 79 (1996), pp. 5955- 5957

[31] M. Saura-Múzquiz, C. Granados-Miralles, H.L. Andersen, M. Stingaciu, M Avdeev, M. Christensen **Nanoengineered High-Performance Hexaferrite Magnets by Morphology-Induced Alignment of Tailored Nanoplatelets** ACS Appl. Nano Mater., 1 (2018), pp. 6938−6949

[32] V. Petříček, M. Dušek, L. Palatinus **Crystallographic Computing System JANA2006: General features** Z. Kristallogr., 229 (2014), pp. 345-352

[33] J. Rodriguez-Carvajal **Recent advances in magnetic structure determination by neutron powder diffraction** Physica B Condens. Matter., 192 (1993), pp. 55-69

[34] **A.N.** Fitch **The High Resolution Powder Diffraction Beam Line at ESRF** J. Res. Natl. Inst. Stand. Technol., 109 (2004), pp. 133-142

[35] C.A. Schneider, W.S. Rasband, K.W. Eliceiri **NIH Image to ImageJ: 25 years of image analysis** Nature methods, 9 (2012), 671-675

[36] R.D. Shannon **Revised effective ionic radii and systematic studies of interatomic distances in halides and chalcogenides** Acta Cryst., A32 (1976), pp. 751-767

[37] J.M.P.J. Verstegen, A.L.N. Stevels **The relation between crystal structure and luminescence in β-alumina and magnetoplumbite phases** Journal of Luminescence, 9 (1979), pp. 406-414

[38] G.K. Williamson, W.H. Hall **X-ray line broadening from filed aluminium and wolfram** Acta Metall., 1 (1953), pp. 22-31

[39] T. Ungar **Characterization of nanocrystalline materials by X-ray line profile analysis** J Mater Sci., 42 (2007), pp. 1584-1593

[40] T.P. Garg, R. Rai, B.K. Singh **Structural characterization of "as-deposited" cesium iodide films studied by X-ray diffraction and transmission electron microscopy techniques** Nuclear Instruments and Methods in Physics Research A, 736 (2014), pp. 128–134

[41] P.E. Kazin, L.A. Trusov, D.D. Zaitsev, Yu.D. Tretyakov, M. Jansen **Formation of submicron-sized $SrFe_{12-x}Al_xO_{19}$ with very high coercivity** Journal of Magnetism and Magnetic Materials, 320 (2008), pp. 1068–1072

[42] J. Qiu, Y. Wang and M. Gu **Effect of Cr substitution on microwave absorption of $BaFe_{12}O_{19}$** Materials Letters, 60 (2006), pp. 2728 – 2732

[43] G. Abo, J. Jalli **Shape Dependent Coercivity Simulation of a Spherical Barium Ferrite (S-BaFe) Particle with Uniaxial Anisotropy** Journal of Magnetics, 17 (2012), pp. 1-5

[44] Z.F. Zi, Y.P. Sun, X.B. Zhu, Z.R. Yang, J.M. Dai, W.H. Song **Structural and magnetic properties of $SrFe_{12}O_{19}$ hexaferrite synthesized by a modified chemical co-precipitation method** Journal of Magnetism and Magnetic Materials, 320 (2008), pp. 2746– 2751

[45] E.A. Gorbachev, L.A. Trusov, A.E. Sleptsova, E.S. Kozlyakova, L.N. Alyabyeva, S.R. Yegiyan, A.S. Prokhorov, V.A. Lebedev, I.V. Roslyakov, A.V. Vasiliev, P.E. Kazin **Hexaferrite materials displaying ultra-high coercivity and sub-terahertz ferromagnetic resonance frequencies** Materialstoday, (2019) https://doi.org/10.1016/j.mattod.2019.05.020

[46] J.C. Faloh-Gandarilla, S. Díaz-Castañón, B.E. Watts **Magnetization reversal and interactions in $SrFe_{12}O_{19}$** Physica status solidi B, 254 (2016), pp. 1–7